PCCP

PAPER

View Article Online
View Journal | View Issue

Cite this: *Phys. Chem. Chem. Phys.*, 2018, **20**, 19458

Photoelectron spectroscopic and computational studies of [EDTA·M(III)]$^-$ complexes (M = H_3, Al, Sc, V–Co)†

Qinqin Yuan,‡§[abc] Xiang-Tao Kong,‡[a] Gao-Lei Hou,[c] Ling Jiang *[a] and Xue-Bin Wang *[c]

Received 9th March 2018,
Accepted 2nd July 2018

DOI: 10.1039/c8cp01548a

rsc.li/pccp

Metal–EDTA complexes commonly exist as biological redox reagents. We have generated a series of such complexes, [EDTA·M(III)]$^-$ (M = Al, Sc, V–Co), *via* electrospray ionization and characterized them by cryogenic mass-selected negative ion photoelectron spectroscopy (NIPES) and quantum chemical computations. Experiments clearly revealed one more spectral band at low electron binding energy for transition metal complexes with d electrons (M = V–Co) compared to those without d electrons (M = Al and Sc). Quantum chemical calculations suggested that all of the metal complexes possess hexacoordinated metal–ligand binding motifs, from which the calculated adiabatic/vertical detachment energy (ADE/VDE) and band gaps are in good agreement with experimental values. Direct spectrum and electronic structure analyses indicted that [EDTA·V(III)]$^-$ can be easily oxidized to [EDTA·V(IV)] with the smallest ADE/VDE of 3.95/4.40 eV among these metal complexes, but further oxidation is hindered by the existence of a 2.30 eV band gap, a fact that accords with the special redox behavior of vanadium-containing species in biological cells. Spin density and molecular orbital analyses reveal that [EDTA·V(III)]$^-$ was overwhelmingly detached from the vanadium atom, in stark contrast to [EDTA·Sc(III)/Al(III)]$^-$, where the detachment occurred from the EDTA ligand. For all other metal complex anions, from M = Cr to Co, the detachment process is derived from contributions from both the metal and ligand. The intrinsic electronic and geometric structures of these complexes, obtained in this work, provide a molecular foundation to better understand their redox chemistries and specific metal bindings in condensed phases and biological cells.

Introduction

Ethylenediaminetetraacetic acid (H_4EDTA) is an interesting and remarkable tetrabasic acid. Its conjugate base, $EDTA^{4-}$, is a ubiquitous electron donor-type ligand, capable of chelating with almost every metal cation in the Periodic Table by two nitrogen atoms and three or four carboxyl groups, forming stable and soluble chelate complexes (see Fig. 1).[1–3] Increasing the EDTA

[a] *State Key Laboratory of Molecular Reaction Dynamics, Dalian Institute of Chemical Physics, Chinese Academy of Sciences, 457 Zhongshan Road, Dalian 116023, China. E-mail: ljiang@dicp.ac.cn*

[b] *University of Chinese Academy of Sciences, 19A Yuquan Road, Beijing 100049, China*

[c] *Physical Sciences Division, Pacific Northwest National Laboratory, 902 Battelle Boulevard, P. O. Box 999, MS K8-88, Richland, Washington 99352, USA. E-mail: xuebin.wang@pnnl.gov*

† Electronic supplementary information (ESI) available: The M–O bond length differences (Å) by subtracting the equatorial bond from the axial bond in the optimized structures of [EDTA·M(III)]$^-$ (M = Al, Sc, V–Co) using five different functionals (Table S1); comparison of experimental ADE/VDE values with calculated ones for all complexes using different functionals (Table S2); comparison of relative energies for the hexadentate [EDTA·M(III)]$^-$ (M = V–Co) complexes of different spin states (Table S3); comparison of relative energies of different isomers for the [EDTA·M(III)]$^-$ (M = Al, Sc, V–Co) complexes (Table S4); Laplacian of electron density ($\nabla^2\rho(r_b)$), and energy density (H_{BCP}) at bond critical points of O–H$\cdots$O hydrogen bonds and hydrogen bonding distance obtained by using the atoms in molecules (AIM) methodology with the Multiwfn program (Table S5); orbital composition analysis of [EDTA·M(III)]$^-$ (M = Al, Sc, V, Cr, Mn, Fe, Co) for HOMOs that contribute to the first peak (X) by the NAO method (Table S6); molecular graph of [EDTA·H_3]$^-$ using the atoms in molecules (AIM) methodology (Fig. S1); molecular orbital pictures (HOMO to HOMO–10) of the most stable isomers for [EDTA·M(III)]$^-$ (M = Al, Sc, V, Cr, Mn, Fe, Co) (Fig. S2); HOMO pictures of the most stable isomers of [EDTA·M(III)]$^-$ (M = Al, Sc, V, Cr, Mn, Fe, Co) (Fig. S3); comparison of the trend of metal atom contribution (%) in HOMOs with the experimental VDEs and ADEs for [EDTA·M(III)]$^-$ (M = Al, Sc, V, Cr, Mn, Fe, Co) (Fig. S4); TDDFT simulated spectra of the lowest isomers for [EDTA·M(III)] (M = H_3, Sc, Mn, Fe, Co) – using five different functionals, in comparison with the corresponding experimental spectra (Fig. S5); Cartesian coordinates for the optimized structures of [EDTA·M(III)]$^-$ (M = Al, Sc, V, Cr, Mn, Fe, Co) and [EDTA·H_3]$^-$ (total 53 pages). See DOI: 10.1039/c8cp01548a

‡ These authors contributed equally to this work.

§ Visiting student supported *via* PNNL alternate sponsored fellowship program.

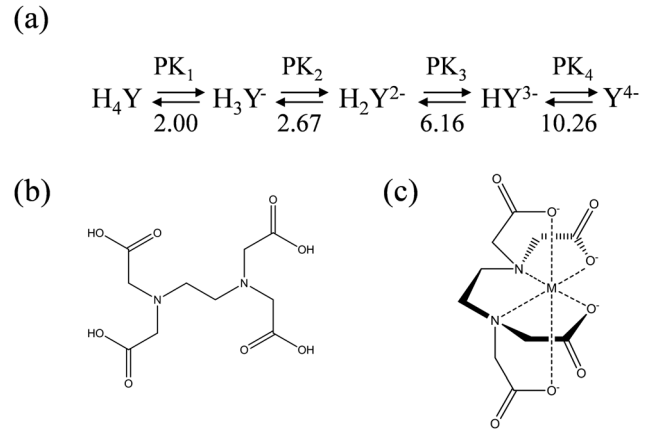

Fig. 1 (a) Acid–base dissociation equilibrium constants of ethylenediaminetetraacetic acid (H_4EDTA), (b) schematic structure of H_4EDTA, and (c) typical binding motif in metal EDTA complexes.

ligand concentration can shift the balance of metal ions among the dissolved, absorbed, and precipitated phases, which consequently can influence the redox potentials of metal ion redox couples and can alter the bioavailability and migration rates of metal ions. Metal–EDTA complexes have been widely used in numerous applications ranging from analytical titrations[4–8] and wastewater treatments[9–15] to biological catalysts,[16–22] as well as in medicine chemistry[23] and in agriculture[24,25] and the food industry.[26] They have also been suggested to play important roles in regulating redox behaviors in biological cells. For instance, several ascidian species are well known as being able to accumulate vanadium in the +5 oxidation state from seawater and to store vanadium in their blood cells in the +3 oxidation state at extremely high levels. During the accumulation process, V^V is reduced to V^{III} *via* V^{IV}.[27,28] Previous research found that cysteine itself cannot reduce V^{IV} to V^{III}, but cysteine ester (CysMe) can reduce V^{IV} to V^{III} with the assistance of EDTA.[29]

Metal–EDTA complexes have been extensively studied using a variety of techniques, including cyclic voltammetry, mass spectrometry,[30,31] EPR,[32,33] NMR,[34–37] FTIR,[1,38,39] FT-Raman spectroscopy,[40,41] and X-ray crystallography.[42,43] These studies have built an extensive body of literature on their geometric structures in crystals and liquids, and shown, in some cases, different coordination modes in different phases. For example, crystalline $[EDTA{\cdot}Fe(III)]^-$ forms approximately pentagonal bipyramidal structures with a hexadentate EDTA and one water molecule coordinated as the seventh ligand, while solution phase $[Fe(III){\cdot}(HEDTA)]$ adopts an overall six-coordinate geometry with a pentadentate EDTA containing one uncoordinated –COOH group and one water molecule occupying the sixth position.[40,44–50] Despite the extensive structural characterizations mentioned above, there have been no reports on probing the intrinsic electronic structures and bonding characters of these ubiquitous complexes in the gas phase, which are the key molecular properties to define and control their biological functionalities, and to understand the underlying redox mechanism and chemistries. In this work, we carry out a combined negative ion photoelectron spectroscopy (NIPES)[51] and quantum chemical computational study on a series of EDTA–metal complexes, $[EDTA{\cdot}M(III)]^-$ (M = Al, Sc, V–Co) as well as $[EDTA{\cdot}H_3]^-$, to probe their intrinsic electronic structures, geometries, and frontier MO properties that are directly relevant to the aforementioned numerous applications of these complexes in solutions and cells.

Experimental methods

The NIPES experiments were performed by using the PNNL cryogenic magnetic-bottle time-of-flight (TOF) photoelectron spectrometer coupled with an electrospray ionization source.[51] $[EDTA{\cdot}H_3]^-$ and $[EDTA{\cdot}Fe(III)]^-$ ions were produced by spraying a freshly prepared ~0.1 mM solution of disodium EDTA salt, and EDTA ferric sodium salt dissolved in mixed H_2O/CH_3CN (1 : 3) solvents, respectively. $[EDTA{\cdot}Co(III)]^-$ was generated by spraying a mixture of ~0.1 mM solution of hexamminecobalt(III) chloride and disodium EDTA salt dissolved in mixed H_2O/CH_3CN (1 : 3) solvents. Other $[EDTA{\cdot}M]^-$ (M = Al, Sc, V, Cr, Mn) complexes were produced by spraying into the gas phase an ~0.1 mM mixture solution of the corresponding metal chloride and disodium EDTA salt dissolved in H_2O/CH_3CN (1 : 3) solvents.

The produced anionic complexes were guided by quadrupole ion guides into a cryogenic 3-D ion trap, where they were accumulated and cooled for 20–100 ms by collisions with cold buffer gas (20% H_2 balanced in helium) before being pulsed out into the extraction zone of a TOF mass spectrometer. In this work, the trap was operated at 20 K to eliminate the possibility of the appearance of extra spectral peaks due to hot bands in the NIPE spectra and to improve energy resolutions. The ions of interest were then each mass-selected and decelerated before being photodetached by a laser beam of 157 nm (7.866 eV) from an F_2 excimer laser. The laser was operated at a 20 Hz repetition rate with the ion beam off at alternating laser shots, enabling shot-to-shot background subtraction to be carried out. Photoelectrons were collected at ~100% efficiency by using a magnetic bottle and analyzed in a 5.2 m long electron flight tube. The recorded TOF photoelectron spectra were converted into electron kinetic-energy spectra by calibration with the known NIPE spectra of I^-[52] and $Au(CN)_2^-$.[53] The electron binding energy (EBE) spectra presented in the paper were obtained by subtracting the electron kinetic energy spectra from the energy of the detaching photons. The energy resolution was about 2% (*i.e.*, ~20 meV for 1 eV kinetic-energy electrons).

Computational methods

Quantum chemical calculations were performed using the Gaussian 09 program suite.[54] Density Functional Theory (DFT) calculations with several different functionals, *i.e.* M06-2X, B3LYP, BHLYP, PBE0, and CAM-B3LYP, were conducted for all $[EDTA{\cdot}M(III)]^-$ complexes. The full calculations using these five different functionals for all systems are provided in the ESI† of this manuscript. Table S1 (ESI†) indicates that geometry optimization using different functionals yields consistent and similar structures for all anion complexes. However, by comparing the calculated vertical/adiabatic detachment energies with the

experimental values, Table S2 (ESI†) shows that M06-2X yielded better results for M = H_3, Al and Sc, but PBE0 worked overall better for M = V–Co. This preference of choice of functionals for energetic calculations, *i.e.*, PBE0 for complexes explicitly containing 3d electrons, and M06-2X for molecules without d electrons, is in accord with recent theoretical studies,[55] and has been commonly practiced.[56–58] Therefore, unless stated otherwise, we present, in the main text, the computational results obtained by employing the M06-2X functional for $[EDTA{\cdot}M(III)]^-$ (M = H_3, Al, Sc) and the PBE0 functional for $[EDTA{\cdot}M(III)]^-$ (M = V, Cr, Mn, Fe, Co). The 6-311+G(d,p) basis set was used for all atoms. Different spin states were also considered for complexes with unpaired 3d electrons (Table S3, ESI†). Structures were optimized using tight convergence criteria without any symmetry restrictions. Harmonic vibrational frequency analyses were carried out to confirm that all structures were real minima. Theoretical vertical detachment energies (VDEs) were calculated as the electronic energy differences between the neutrals and anions both at the optimized anion geometries, while theoretical adiabatic detachment energies (ADEs) were calculated as the electronic energy differences between the neutral and anion at each optimized geometry and including zero-point energy corrections. The excited state energies of the neutral complexes, accessible *via* photodetaching the corresponding anions, were calculated using time-dependent DFT (TDDFT) at the anion's geometries. In light of the known fact that different methods can, in many cases, give rise to different calculated results,[55–61] in particular, several recent theoretical studies have shown the inaccuracy of the M06 method,[59–61] we compare the simulated spectra using different methods with the experimental spectra in the computational results and discussion section F.

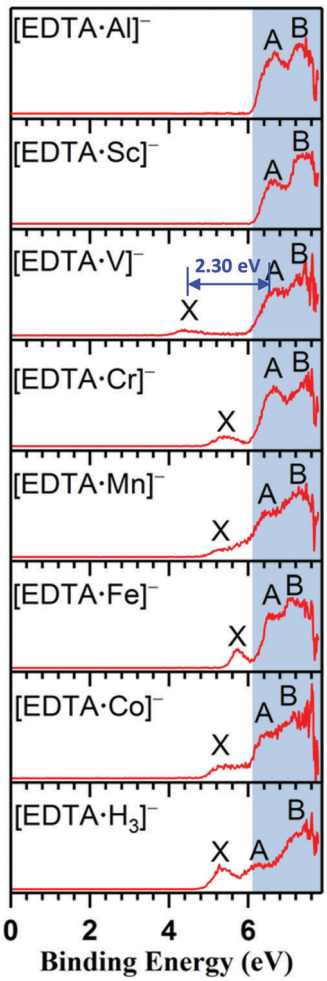

Fig. 2 Low-temperature (20 K) photoelectron spectra of $[EDTA{\cdot}H_3]^-$ and $[EDTA{\cdot}M(III)]^-$ (M = Al, Sc, V–Co) at 157 nm (7.866 eV).

Experimental results

Fig. 2 presents the 20 K 157 nm NIPE spectra of $[EDTA{\cdot}H_3]^-$ and $[EDTA{\cdot}M]^-$ (M = Al, Sc, V–Co). Two spectral bands, labeled as A and B in the EBE range of 6.0–7.5 eV, can be seen in the M = Al and Sc spectra; and, there is an extra feature X at a lower EBE with relatively low intensity that appears for each M = H_3 and V–Co complex besides the A and B bands. These observed bands represent the transitions from the electronic ground state of the anions to the ground and excited states of the corresponding neutrals. There is a one-to-one correspondence between the spectral peaks (X, A and B) among all metal EDTA complexes, as labeled in Fig. 2, except for the absence of peak X in the spectra of $[EDTA{\cdot}Al(III)]^-$ and $[EDTA{\cdot}Sc(III)]^-$ that do not have excess d electrons on the metal centers. The experimental 1st VDE values, estimated from the first peak maximum in each spectrum, are 6.65 ± 0.10, 6.65 ± 0.10, 4.40 ± 0.10, 5.40 ± 0.10, 5.32 ± 0.10, 5.72 ± 0.10, 5.50 ± 0.20, and 5.35 ± 0.10 eV for $[EDTA{\cdot}M]^-$ (M = Al, Sc, V, Cr, Mn, Fe, Co), and $[EDTA{\cdot}H_3]^-$ (Table 1), respectively. Since no vibrational features were resolved in the spectrum, the experimental ADE was estimated by drawing a straight line along the leading edge of the threshold band and then adding the instrumental resolution (fwhm) to the electron binding energy at the crossing point between the line and the EBE axis. The ADE values are 6.10 ± 0.10, 6.25 ± 0.10, 3.95 ± 0.10, 4.90 ± 0.10, 4.85 ± 0.10, 5.40 ± 0.10, 4.85 ± 0.10, and 4.80 ± 0.10 eV for $[EDTA{\cdot}M]^-$ (M = Al, Sc, V, Cr, Mn, Fe, Co) and $[EDTA{\cdot}H_3]^-$ (Table 1), respectively. Among all of the complexes, $[EDTA{\cdot}V(III)]^-$ possesses the lowest ADE/VDE (3.95/4.40 eV) and the biggest X–A energy gap (~2.30 eV); $[EDTA{\cdot}Fe(III)]^-$ has the highest ADE/VDE (5.40/5.72 eV) among those with d electrons.

Computational results and discussion

Quantum chemical calculations were carried out to elucidate the geometric and electronic structures of the EDTA–metal complexes, and to assign the observed spectral bands. The optimized structures for the $[EDTA{\cdot}H_3]^-$ and $[EDTA{\cdot}M(III)]^-$ anions and their corresponding $[EDTA{\cdot}H_3]$ and $[EDTA{\cdot}M(III)]$ neutrals are shown in Fig. 3 with their key bond lengths listed in Table 2. The calculated ADEs/VDEs for the most stable isomers are given in Table 1 in comparison with the experimental values. The excitation energies were obtained by TDDFT calculations, and the resultant simulated spectra based on the lowest isomers are compared with the experiments in Fig. 4.

Table 1 Experimental adiabatic/vertical detachment energies (ADEs/VDEs), X–A energy gap (ΔE), and calculated ADEs/VDEs for $[EDTA{\cdot}H_3]^-$ and $[EDTA{\cdot}M(III)]^-$ (M = Al, Sc, V–Co) (in eV)

	M	H_3	Al	Sc	V	Cr	Mn	Fe	Co
Expt. ADE[a]		4.80(10)	6.10(10)	6.25(10)	3.95(10)	4.90(10)	4.85(10)	5.40(10)	4.85(10)
Expt. VDE[a]	X	5.35(10)			4.40(10)	5.40(10)	5.32(10)	5.72(10)	5.50(20)
	A	6.20(20)	6.65(10)	6.65(10)	6.70(10)	6.65(10)	6.50(10)	6.60(10)	6.50(10)
	B	~7.20	7.30(10)	7.40(10)	~7.20	~7.35	~7.20	7.10(10)	~7.20
Calc. VDE[b]	Iso I[c]	5.32	6.62	6.67	4.47	5.47	5.12	5.61	5.41
	Iso II	5.43							5.69
	Iso III	5.32							
Calc. ADE[b]	Iso I	4.80	5.62	5.80	3.85	4.86	4.40	5.26	5.11
Expt. ΔE		0.85	0.65	0.75	2.30	1.25	1.18	0.88	1.00

[a] Numbers in parentheses represent experimental uncertainties in the last digits. [b] M06-2X/6-311+G(d,p) values for $[EDTA{\cdot}H_3]^-$ and $[EDTA{\cdot}Al/Sc]^-$; PBE0/6-311+G(d,p) values for $[EDTA{\cdot}M]^-$ (M = V–Co). [c] See Fig. 3 for the structures of different isomers.

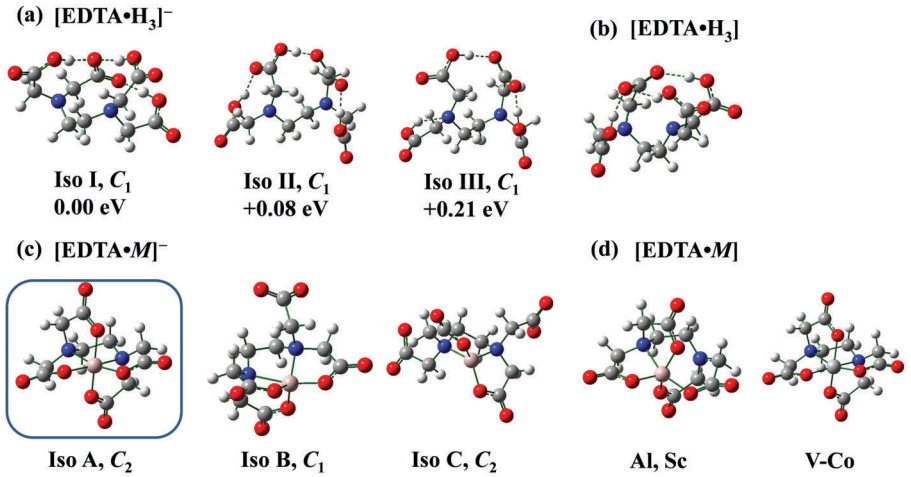

Fig. 3 Optimized structures of $[EDTA{\cdot}H_3]^-$, $[EDTA{\cdot}M(III)]^-$, and their corresponding neutrals (M = Al, Sc, V–Co) (H, light grey; C, dark gray; O, red; N, blue).

Table 2 Selected bond lengths (Å) for the optimized structures of $[EDTA{\cdot}M(III)]^{-/\bullet}$ (M = Al, Sc, V–Co)

		Al(III)[a]		Sc(III)[a]		V(III)[b]		Cr(III)[b]		Mn(III)[b]		Fe(III)[b]		Co(III)[b]	
EDTA·M(III)		Anion ^1A	Neutral ^2A	Anion ^1A	Neutral ^2A	Anion ^3A	Neutral ^2A	Anion ^4A	Neutral ^3A	Anion ^5A	Neutral ^4A	Anion ^6A	Neutral ^5A	Anion ^1A	Neutral ^2A
Axial	M–O(21) (Å)	1.889	1.835	2.074	2.167	1.977	1.889	1.958	1.857	1.906	1.875	2.004	1.844	1.901	1.838
	M–O(31) (Å)	1.889	1.806	2.074	1.995	1.977	1.889	1.958	1.857	1.906	1.875	2.004	1.844	1.901	1.838
Equatorial	M–O(7) (Å)	1.834	1.89	2.046	1.984	1.985	1.852	1.974	1.85	1.961	1.845	1.946	1.872	1.898	1.84
	M–O(16) (Å)	1.834	1.773	2.046	2.004	1.985	1.852	1.974	1.85	1.961	1.845	1.946	1.872	1.898	1.84
Equatorial	M–N(1) (Å)	2.137	2.782	2.35	2.318	2.185	2.168	2.099	2.118	2.325	2.055	2.252	2.239	1.949	1.98
	M–N(10) (Å)	2.137	2.061	2.35	2.898	2.185	2.168	2.099	2.118	2.325	2.055	2.252	2.239	1.949	1.98

[a] M06-2X/6-311+G(d,p) values. [b] PBE0/6-311+G(d,p) values.

A. Optimized structures of $[EDTA{\cdot}H_3]^-$ and $[EDTA{\cdot}H_3]^\bullet$. Three low energy isomers with the singlet ground state (^1A) and C_1 symmetry are identified for $[EDTA{\cdot}H_3]^-$. In the most stable isomer (Iso I), one oxygen from the carboxylate group ($-COO^-$) acts as a double acceptor forming two hydrogen bonds (HBs) with two carboxylic groups (–COOH), and the other O atom forms a third HB with the remaining –COOH group (Fig. 3). The next low-lying isomer (Iso II, +0.08 eV) can be viewed as constructed *via* the formation of three O–H···O HB chains in a relay fashion among three carboxylic and one carboxylate groups. In Iso III (+0.21 eV), the $-COO^-$ end forms two O–H···O HBs with two –COOH groups in vicinity, and the remaining –COOH interacts with an amine to form an O–H···N HB. For the optimized neutral, three O–H···O HBs are formed between

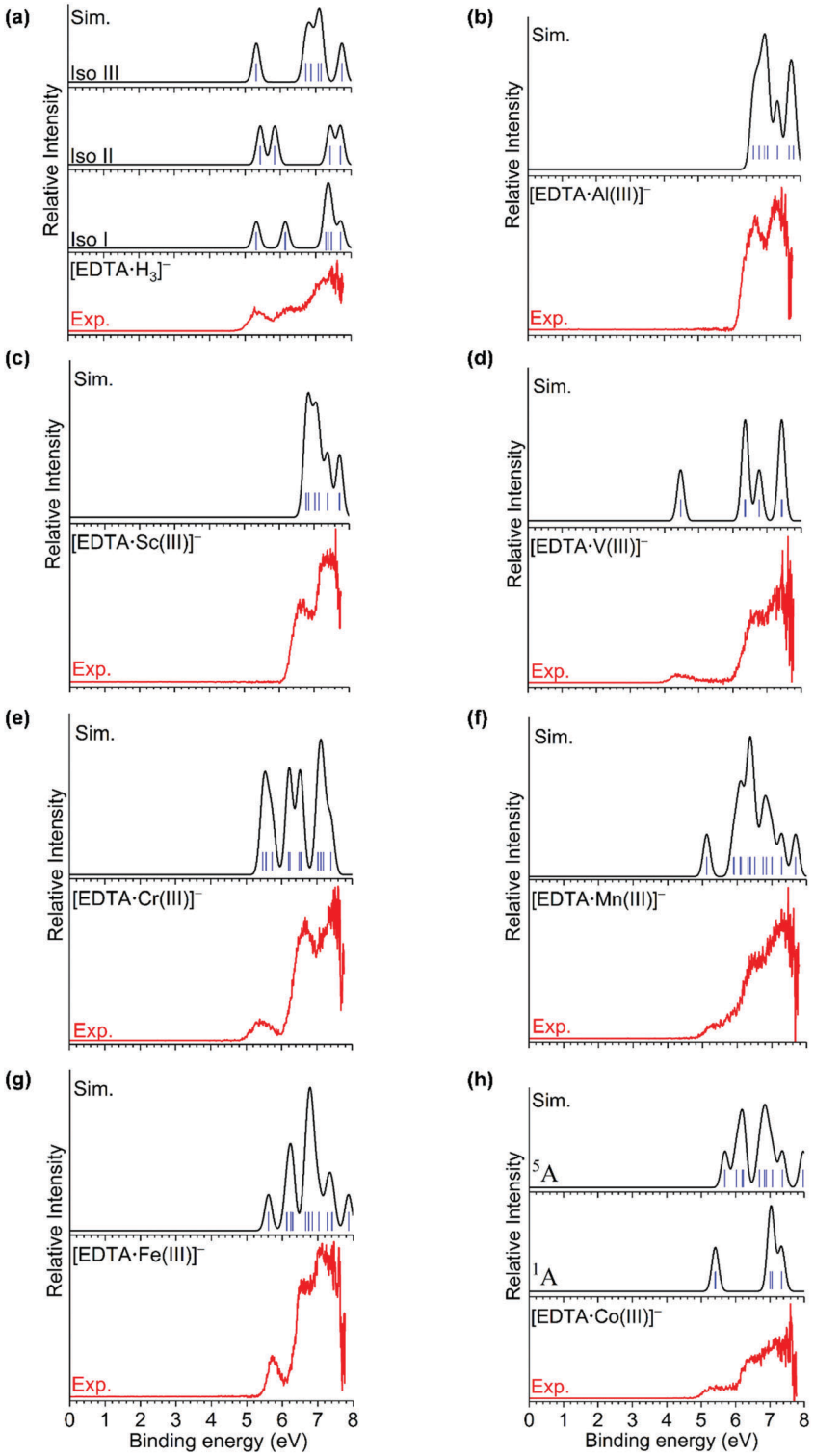

Fig. 4 TDDFT simulated spectra of the lowest energy isomers for $[EDTA{\cdot}H_3]^-$ (a) and $[EDTA{\cdot}M(III)]^-$ (M = Al, Sc, V–Co) (b–h), in comparison with the corresponding experimental spectra.

the –COO• group and three neighboring –COOH groups with one of the O atoms acting as a double acceptor. The formation of multiple HBs is confirmed by the quantum theory of atoms in molecules (QTAIM) using the Multiwfn program[62] (see Fig. S1 and Table S5 in the ESI†).

B. Calculated ADEs/VDEs and simulated NIPE spectra for $[EDTA{\cdot}H_3]^-$. The M06-2X/6-311+G(d,p) calculated ADE of 4.80 eV, and VDEs of 5.32, 5.43, and 5.32 eV for Iso I–III, respectively, are in excellent agreement with the corresponding experimental values of 4.80, and 5.35 eV (Table 1). The TDDFT predicted

spectra based on Iso I, II, and III are displayed in Fig. 4, and they provide a qualitative comparison for, and not a numerical confirmation of, the experimental spectra. The spectrum of Iso I exhibits three main peaks, centered at 5.30, 6.20, and 7.30–7.70 eV, respectively. Similarly, the Iso II spectrum shows three spectral bands at 5.40, 5.80, and 7.40–7.70 eV. Combining these predicted bands from both isomers leads to a reasonable fit to the experimental spectrum, except that the predicted third bands that start at EBE $>$ 7.00 eV are $\sim$0.30 eV higher than the experimental onset value of 6.80 eV. The spectrum of Iso III (+0.21 eV), which has three predicted bands with the second one present in the region of EBE = 6.40–7.40 eV, may contribute to the rising edge of feature B. Therefore, we suggest that all of the three isomers coexist in the experiments and contribute to the observed $[EDTA{\cdot}H_3]^-$ spectrum. Because each isomer contains three O–H$\cdots$O HBs, $[EDTA{\cdot}H_3]^-$ should have a much higher EBE than the isolated carboxylate ($\sim$3.50 eV).[63] This expectation is borne out in our experiments, and further confirmed by our calculations.

C. Optimized structures of $[EDTA{\cdot}M(III)]^{-/\bullet}$ (M = Al, Sc, V–Co). We first considered quasi-octahedral structures of $[EDTA{\cdot}M(III)]^-$ with hexadentate EDTA–M bonds (Iso A, Fig. 3), because this type of binding motif was commonly reported in previous crystallographic studies.[64,65] Next, different geometries including pentadentate (Iso B, Fig. 3) and tetradentate (Iso C, Fig. 3) EDTA–M coordination were also optimized, but they were found to be at least 1 eV higher in energy than Iso A (Table S4, ESI†), too high to be generated under our experimental conditions. Accordingly, all of the $[EDTA{\cdot}M(III)]^-$ (M = Al, Sc, V–Co) anions studied here possess distorted octahedral coordination geometries with C_2 symmetry and hexadentate EDTA ligands, in which two N atoms from amines and two O atoms from one carboxylate occupy the four equatorial positions, while two oxygens from the second carboxylate reside at the two axial positions. Similar octahedral complexes were reported in $(NH_4)[Al(EDTA)]{\cdot}2H_2O$ and $K[Al(EDTA)]{\cdot}2H_2O$ crystals.[64,65] It should be pointed out that different EDTA−M structures rather than the octahedron have been observed in the solution phase; for instance, a penta-coordinated trigonal bipyramidal structure was proposed for $[EDTA{\cdot}Al(III)]^-$,[66] and a heptacoordinate complex with one water and a hexadentate EDTA ligand was suggested for $[EDTA{\cdot}Fe(III)]^-(H_2O)$.[40] The $[EDTA{\cdot}M(III)]^-$ complexes are closed shells for M = Al and Sc, while for M = V–Co, they have unpaired 3d electrons. Therefore, different spin states were calculated and they are compared in Table S3 (ESI†) for $[EDTA{\cdot}M(III)]^-$ (M = V–Co). The results show that high spin states are favored for the complexes of M = V to Fe with low spin states being at least 0.85 eV higher in energy, with one exception for the Co species, of which the singlet state is energetically 0.37 eV more stable than the quintet state.

Selected bond lengths of the optimized pseudo octahedral structure (Iso A) of $[EDTA{\cdot}M(III)]^-$ (M = Al, Sc, V–Co) in each respective ground electronic state are given in Table 2. All M–N bond lengths are longer than M–O bond lengths due to the lower electronegativity of N as against O. The M = V, Cr and Mn EDTA anions are compressed octahedrons, in which the axial M–O distances are shorter on average than the equatorial M–O distances, while the reverse holds for the other metal complexes (M = Al, Sc, Fe and Co) that are elongated octahedrons, in which the axial M–O distances are longer than that in the equatorial plane. Previous X-ray measurements showed that the equatorial M–O bonds were longer on average than the axial ones for $[EDTA{\cdot}Cr(III)]^-$ and $[EDTA{\cdot}Co(III)]^-$, for which the ligand field stabilization (LFS) appeared significant, while the reverse held for $[EDTA{\cdot}Fe(III)]^-$ and $[EDTA{\cdot}Al(III)]^-$, for which there was no appreciable LFS contribution.[46] Our calculated structures for M = Al, Cr, Fe are consistent with those determined in the solids, but for $[EDTA{\cdot}Co(III)]^-$, its predicted gas phase structure is different from that in the solid state.

The corresponding neutral complexes were also optimized. Comparison of the anionic and neutral structures of $[EDTA{\cdot}M(III)]^{-/\bullet}$ (M = V–Co) reveals overall minor geometric changes in terms of structural binding motifs upon electron detachment, but changes significant enough in key bond lengths to alter the overall shapes of the octahedrons, *i.e.* compressed anions $\rightarrow$ elongated neutrals and elongated anions $\rightarrow$ compressed neutrals (Table 2). The neutral M–O distances decrease, presumably due to the enhanced M(IV)–O bonds. Interestingly, upon one electron detachment, the M–N bond length exhibits a variation ranging from significantly shortened for Mn (−0.27 Å) to slightly shortened for V (−0.02 Å), Fe (−0.01 Å), and to modestly lengthened for Cr (+0.10 Å) and Co (+0.03 Å) (Table 2), among which the change of the Mn–N distance is the biggest. The underlying reasons for this ominous Mn–N bond length change will be discussed in the next sections *via* analyzing electron spin density and molecular orbitals. For the closed shell anions $[EDTA{\cdot}Al]^-$ and $[EDTA{\cdot}Sc]^-$, electron detachment leads to the neutral radical complexes, in which EDTA becomes pentadentate, leaving one N atom uncoordinated (Fig. 3).

D. Strain energies in EDTA and metal–ligand interaction energies. The dominant driving force in forming $[EDTA{\cdot}M(III)]^-$ complexes is the strong M^{3+}–$EDTA^{4-}$ metal ligand interaction, which binds metals and EDTA together and overcomes the subsequent ligand distortion energy and Coulomb repulsion between negatively charged groups. The final structures are

Table 3 Calculated strain and interaction energies (eV) for $[EDTA{\cdot}M(III)]^-$ (M = Al, Sc, V–Co)

EDTA·M(III)	Al(III)	Sc(III)	V(III)	Cr(III)	Mn(III)	Fe(III)	Co(III)
Strain energy[a]	7.35	5.99	6.54	6.72	6.74	6.44	7.54
Interaction energy[b]	−80.55	−71.49	−76.43	−78.58	−79.02	−77.34	−86.36

[a] Calculated as the energy difference between $[EDTA]^{4-}$ adopting the same geometry as in the optimized $[EDTA{\cdot}M]^-$ complex and in its isolated free form. [b] Energy difference between $[EDTA{\cdot}M]^-$ and the sum of free M and EDTA.

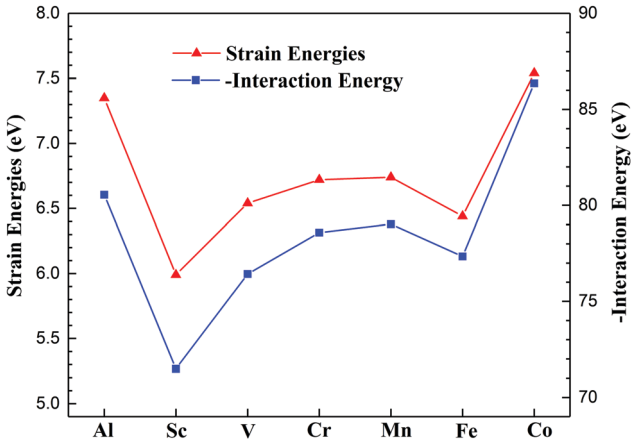

Fig. 5 Trend of calculated strain energies compared with the interaction energies for [EDTA·M(III)]$^-$.

largely determined by the overall balance in the energy landscapes, which can change the structure of the free ligand by bending the carboxylic chains to bring them closer, which otherwise would tend to stay as far away as possible without M^{3+}. A stronger metal ligand interaction is expected to give rise to a larger ligand strain energy. A quantitative description of the degree of distortion of the bent $[EDTA]^{4-}$ in the optimized geometries of $[EDTA{\cdot}M(III)]^-$ is displayed in Table 3 and Fig. 5, where the ligand strain energy and the metal–EDTA interaction strength exhibit a good correlation, similar to that in alkali metal dicarboxylate complexes reported by our group.[67]

E. Calculated ADEs/VDEs and simulated spectra for $[EDTA{\cdot}M(III)]^-$ (M = Al, Sc, V–Co). The calculated ADEs/VDEs for the lowest energy isomers of $[EDTA{\cdot}M(III)]^-$ (M = Al, Sc, V–Co) are 5.62/6.62, 5.80/6.77, 3.85/4.47, 4.86/5.47, 4.40/5.12, 5.26/5.61, and 5.11/5.41 (5.69) eV for M = Al, Sc, V, Cr, Mn, Fe, Co (singlet/quintet), respectively, in good agreement with the corresponding experimental values of 6.10/6.65, 6.25/6.65,

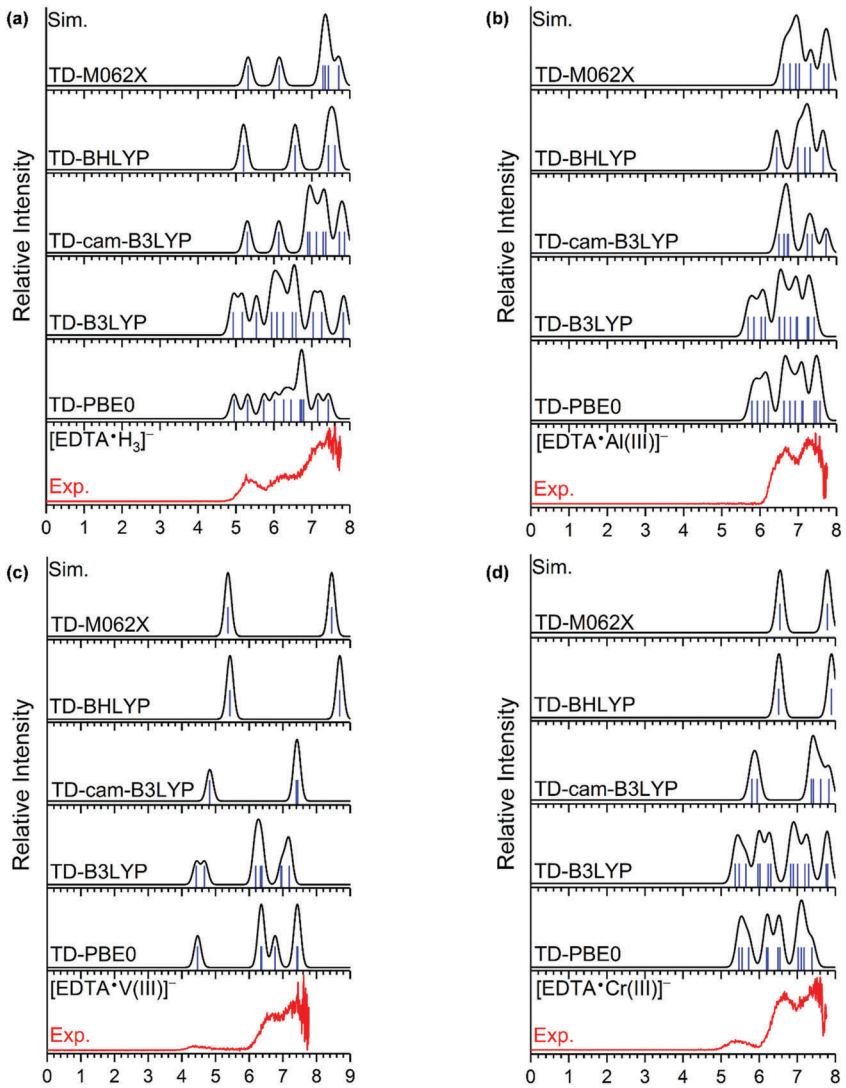

Fig. 6 TDDFT simulated spectra of the lowest energy isomers for $[EDTA{\cdot}H_3]^-$ (a), $[EDTA{\cdot}M(III)]^-$ M = Al (b), V (c), and Cr (d) using five different methods, in comparison with the corresponding experimental spectra.

3.95/4.40, 4.90/5.40, 4.85/5.32, 5.40/5.72 and 4.85/5.50 eV (Table 1). To determine whether the other isomers coexist in the experiments and contribute to the experimental spectra, TDDFT excitation energies were computed and simulated spectra by Gaussian broadening of the stick spectra were generated. For the $[EDTA{\cdot}M(III)]^-$ complexes (M = Al, Sc, and V–Fe, except Co), the simulated spectra of the lowest energy isomers agree very well with the experimental spectra (Fig. 4), indicating that only the most stable isomers, *i.e.*, octahedral structures with hexadentate EDTA (Iso A), contribute to the experiment. For $[EDTA{\cdot}Co(III)]^-$, the simulated spectrum of the lowest energy isomer (Iso A with ^1A state) shows a clear 1.50 eV band gap between two peaks at 5.50 and 7.00 eV, apparently missing the 2nd spectral band in comparison to the experiment. However, the absent peak in the simulated spectrum from the ^1A state can be recovered by including the quintet Iso B (Fig. 4). The calculated VDEs for both ^1A and ^5A states, 5.41, and 5.69 eV, as already mentioned, agree with the experimental value (5.50 ± 0.20 eV). Therefore, we suggest that both isomers with ^1A and ^5A states coexist and contribute to the experiments.

F. Comparison of the method-based simulated spectra with the experimental ones. Fig. 6 shows the TD-DFT simulated spectra using DFT = M06-2X, BHLYP, CAM-B3LYP, B3LYP, and PBE0 methods for M(III) = H_3, Al, V and Cr in comparison with their respective experimental ones (the comparison for all other complexes is provided in Fig. S5 in the ESI†). It can be seen that different methods give rise to a series of simulated spectra varied in both peak positions and spectral patterns. Overall, the M06 method yields the best fit to the experiments for M = H_3, Al, and Sc, while PBE0 and B3LYP provide a good fit to the spectra for M = V–Co. The existence of the large X–A band gap in the V case, however, is confirmed by all calculations. Fig. 6 and Fig. S5 (ESI†) highlight the importance of obtaining experimental results to benchmark different theoretical methods.

G. Theoretical analyses on the nature of the first detachment band for $[EDTA{\cdot}M(III)]^-$ (M = Al, Sc, V–Co). Electron spin density differences between $[EDTA{\cdot}M(III)]^{\bullet}$ neutrals and $[EDTA{\cdot}M(III)]^-$ anions at the optimized anionic geometries were computed, in order to obtain a qualitative picture showing where the least bound electrons are detached (Fig. 7). It can be concluded that for Al and Sc, the electron is detached from the O atoms of the EDTA ligand, in contrast to the M = V case, in which majority of detached electrons come from V(III) atoms. For the other $[EDTA{\cdot}M(III)]^-$ complexes (M = Cr, Mn, Fe, Co), both the ligand and metal contribute significantly to the lowest electron detachment channel.

Our TDDFT calculations, shown in Fig. 4, indicate that the first peak involves a one electronic state transition for the metal complexes M = V and Mn, but it involves multiple electronic states for M = Al, Sc, Cr, Fe, Co. Fig. 8 depicts the relevant occupied molecular orbitals that contribute to the observed lowest binding energy peaks (X for M = V–Co, A for M = Al, Sc). Four electronic state transitions are involved in the A band of the M = Al and Sc spectra, corresponding to detached electrons from HOMO to HOMO–3 under the single particle picture approximation. The percentage of metal atoms (Al and Sc) is

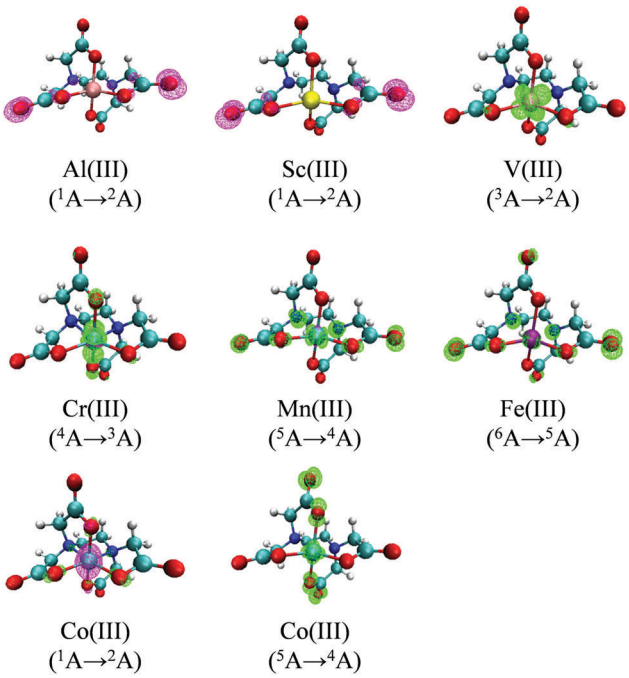

Fig. 7 Electron spin density difference between $[EDTA{\cdot}M(III)]^{\bullet}$ and $[EDTA{\cdot}M(III)]^-$ at the optimized anionic geometries based on Mulliken population analysis (M = Al, Sc, V–Co) (isovalue = 0.01).

only 2% or less for these four MOs, which accords with the finding that the electron detachment mainly comes from the ligand. For $[EDTA{\cdot}V(III)]^-$, only one transition is involved in the X peak, which corresponds to detaching one electron from the HOMO, which possesses a 66.2% contribution from the metal, in contrast to the M = Al and Sc cases. For the other complexes, the metal contribution to the first peak decreases in the order of Cr (41.3%, HOMO−1) > Mn (14.6%, HOMO) > Fe (8.3%, HOMO−2) > ^5A state of Co (5.6%, HOMO−1). Therefore, it is clear that the frontier MOs of the M = V–Co species always have d electron contributions from the metals, while the M = Al and Sc complexes do not. This conclusion from the MO analyses is exactly the same as that drawn from the electron spin density analyses.

Previous studies of $[Fe(III)X_4]^-$ *vs.* $[Sc(III)X_4]^-$ (X = Cl, Br) revealed appreciably smaller VDEs of the former compared to the latter, presumably due to the fact that the electrons were detached from the Fe 3d orbitals in the case of Fe while they were detached from the halide ligands in the case of Sc.[68,69] We found that the $[EDTA{\cdot}M(III)]^-$ (M = Al, Sc) complexes have extremely large VDEs of 6.65 eV, in contrast to the VDE of 4.40 eV for $[EDTA{\cdot}V(III)]^-$, which is consistent with the previous studies. In fact, we found that there exists a good anti-correlation between VDE and metal 3d contributions (Table S6, ESI†). For the other metal complexes (M = Cr, Mn, Fe, Co), since the loosely bound electron is detached from both the metal and ligand, their VDEs are located in between $[EDTA{\cdot}V(III)]^-$ and $[EDTA{\cdot}Sc/Al(III)]^-$. One exception shown in Fig. S3 (ESI†) is that the VDE of Mn(III) is unexpectedly smaller than that of Cr(III), despite the fact that the HOMO of the former contains much

less d contributions than the latter. A close examination of the HOMO of [EDTA·Mn(III)]$^-$ indicates a significant increase from the N atoms in the ligand (30.6% N, 42.6% O for Mn *vs.* 1.3% N, 53.1% O for Cr), which suggests that both amino and carboxylate moieties are contributing to the X band. Since electron detachment from the amino moiety is much easier than from the carboxylate moiety (for example, VDE = 4.00 eV for $C_6H_5COO^-$; 1.50 eV for $C_6H_5NH^-$),[70,71] the increased N contribution in the HOMO provides a reasonable rationale for the observed lower VDE for [EDTA·Mn(III)]$^-$.

As detailed above, [EDTA·M(III)]$^-$ (M = Al and Sc) formally has no 3d electrons on the metal center for Al^{3+} and Sc^{3+}, so the extra electron must be detached from the EDTA ligand. The rest of the complexes [EDTA·M(III)]$^-$ (M = V–Co) can be assumed to have a partial 3d electron detachment. We found that the forth ionization energies of V–Co, *i.e.*, V (46.71 eV) < Cr (49.16 eV) < Mn (51.20 eV) < Fe (54.80 eV) > Co (51.30 eV),[72] are in a similar trend with the observed trend of VDEs. Of course, this is a very rough approximation without even considering the ligand field influence. According to Crystal Field Theory, ligands often

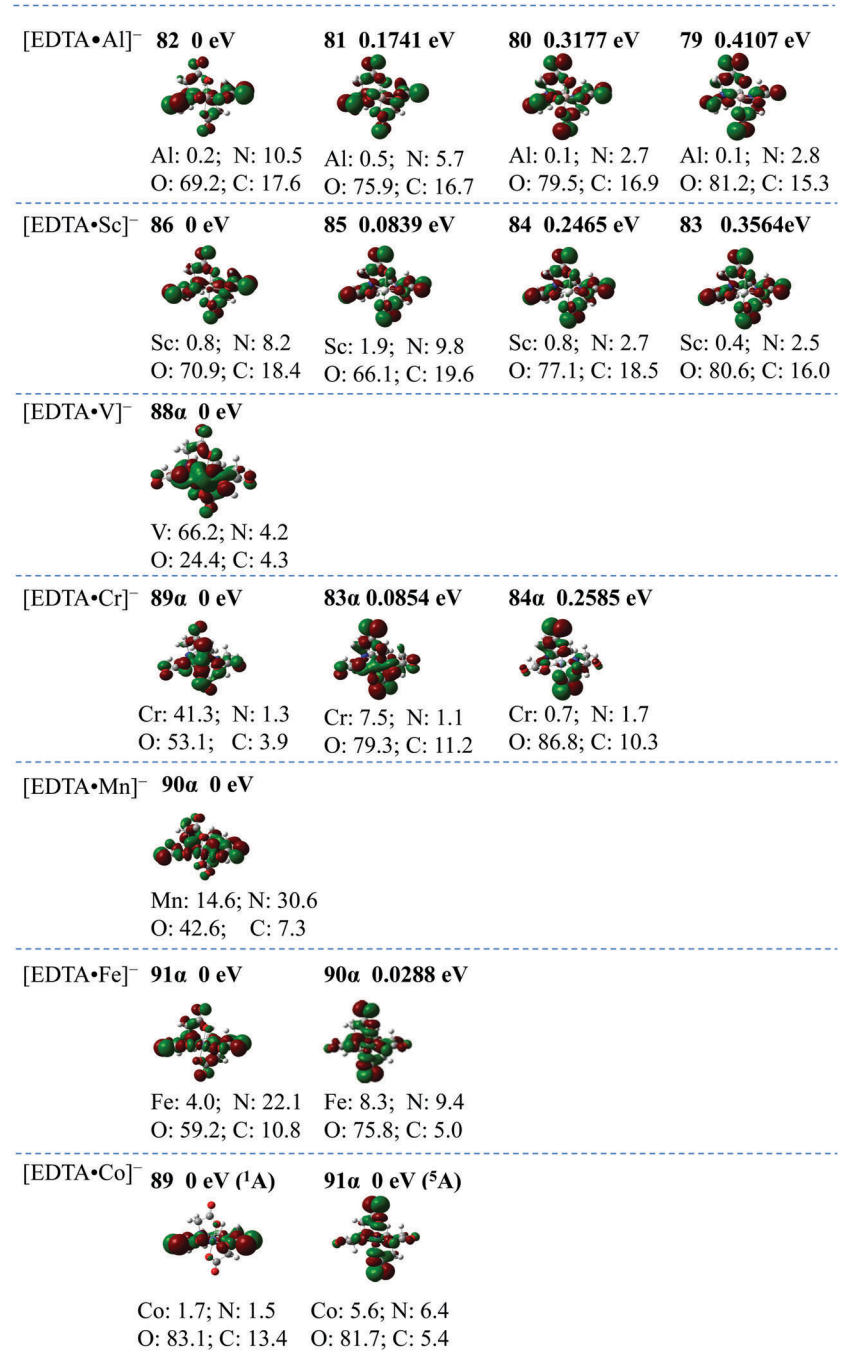

Fig. 8 Frontier molecular orbital analyses for those that contribute to the first peak (X) in the [EDTA·M(III)]$^-$ (M = Al, Sc, V–Co) spectra.

cause a large splitting Δ between T_{2g} and E_g sets of d-orbitals when they form octahedral complexes. The sextet [EDTA·Fe(III)]$^-$ was shown to have a higher ADE/VDE (5.40/5.72 eV) than the others, a fact that is also related to the more stable half-filled d shell (^6A: $T_{2g}^3E_g^2$) that this complex has. On the other hand, [EDTA·Mn(III)]$^-$, a quintet state (^5A) with the $T_{2g}^3E_g^1$ configuration, is able to relatively easily lose one electron to form a relatively stable T_{2g}^3 configuration, compared to its neighbors [EDTA·Cr(III)]$^-$ (^4A, T_{2g}^3) and [EDTA·Fe(III)]$^-$ (^6A, $T_{2g}^3E_g^2$).

H. Implications for EDTA–metal redox chemistry. Photodetachment is an oxidation process, analogous to a half redox reaction (because there is no electron acceptor involved),[68] therefore the NIPE spectrum contains important and explicit electronic structural information about the electron transfer of redox species in the gas phase. Among all [EDTA·M(III)]$^-$ complexes studied here, the triplet state V(III) species with a d^2 electronic configuration has the lowest ADE (3.95 eV), the closed shell Al(III)/Sc(III) anions without d electrons have the highest ADE values (6.10/6.20 eV), while the other metal complexes (M = Cr–Fe) with 3d electrons have ADEs in between. Therefore, our experiments provide a direct indication that the intrinsic oxidation potential $E_{1/2}$ to remove (donate) one electron from the anionic complex follows in the order of V < Cr–Fe < Al (Sc), as shown for the trends of ADE/VDE in Fig. 9. Another salient point observed in the V(III) spectrum is that there exists a 2.30 eV band gap between the ground and first excited states, which, in a qualitative picture, suggests the stability of the V(IV) state with a d^1 configuration and with further oxidizing V(IV) to V(V) being very difficult. Such electronic information obtained from the [EDTA·V(III)]$^-$ spectrum can help in elucidating the special nature of the V^{IV}/V^{III} redox couple and may explain why cysteine itself cannot reduce V^{IV} to V^{III}, but cysteine methyl ester can reduce V^{IV} to V^{III} with the assistance of EDTA in the vanadocytes of ascidians.[29] The biggest energy gap (2.30 eV) of [EDTA·V(III)]$^-$ observed in Fig. 2 and Table 1 is quite unique, in that we could not observe such a large energy gap for the other complexes. This indicates the large stability of the d^1 electron configuration in [EDTA·V(IV)], which is consistent with the stability constant of $[VO(EDTA)]^{2-}$ ($\log K$ = 18.63) being larger than that of $[VO_2(EDTA)]^{2-}$ ($\log K$ = 15.55).[73]

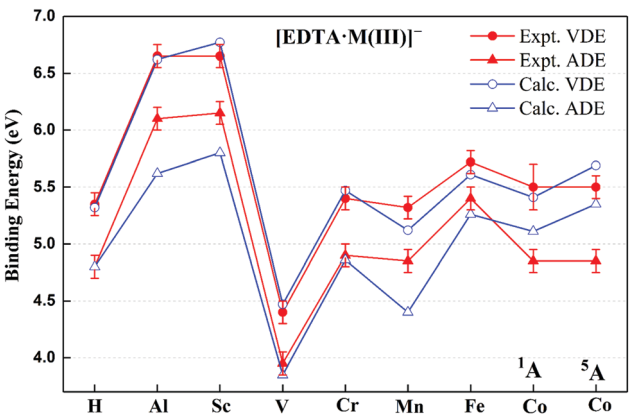

Fig. 9 Comparison of experimental and calculated VDEs and ADEs for [EDTA·H_3]$^-$ and [EDTA·M(III)]$^-$ (M = Al, Sc, V–Co).

Conclusions

In summary, we report a joint NIPES and computational study on the electronic and geometrical structures of a series of EDTA complexes [EDTA·M(III)]$^-$ (M = H_3, Al, Sc, V–Co) that are commonly observed in condensed phases. Except for M = H_3, all metal complexes adopt pseudo-octahedral structures with hexadentate ligands. The experiments clearly showed that there is one more spectral band at a considerably lower EBE for the transition metal complexes with extra d electrons in comparison to those without d electrons (M = Al and Sc), and hence, the intrinsic oxidation potential $E_{1/2}$ follows in the order of V < Cr–Fe < Al (Sc). The spin density and MO orbital composition analyses revealed that the electron detachment channel varies across the third row metals, and there exists a good anti-correlation between the $E_{1/2}$ and metal contribution in the frontier MOs. The observation of a much lower ADE and existence of a large band gap in [EDTA·V(III)]$^-$ may help to elucidate the special redox behavior of vanadium species in biological cells. The intrinsic molecular properties of these complexes obtained in this work provide a molecular foundation to better understand their numerous applications, redox chemistries, and biological functions in condensed phases.

Conflicts of interest

The authors declare that there are no conflicts of interest.

Acknowledgements

The experimental work was supported by the U.S. Department of Energy (DOE), Office of Science, Office of Basic Energy Sciences, Division of Chemical Sciences, Geosciences and Biosciences, and was performed using EMSL, a national scientific user facility sponsored by the DOE's Office of Biological and Environmental Research and located at Pacific Northwest National Laboratory, which is operated by Battelle Memorial Institute for the DOE. The computational work was supported by the National Natural Science Foundation of China (Grant No. 21688102) and the Strategic Priority Research Program (Grant No. XDB17000000) of the Chinese Academy of Science and conducted on the clusters of the Center for Theoretical and Computational Chemistry at the Dalian Institute of Chemical Physics. We would like to gratefully acknowledge one of the anonymous reviewers for his/her excellent suggestion to present simulated spectra based on different methods in comparison to the experimental ones, so the readers can clearly see and have better judgment on the performance of the methods employed.

References

1 K. Nakamoto, Y. Morimoto and A. E. Martell, *J. Am. Chem. Soc.*, 1963, **85**, 309–313.
2 R. Nuttall and D. Stalker, *Talanta*, 1977, **24**, 355–360.
3 B. E. Douglas and D. J. Radanović, *Coord. Chem. Rev.*, 1993, **128**, 139–165.
4 J. H. Yoe, *J. Am. Chem. Soc.*, 1958, **80**, 2600.
5 E. W. Baumann and R. M. Wallace, *Anal. Chem.*, 1969, **41**, 2072–2074.
6 E. T. Clarke and A. E. Martell, *Inorg. Chim. Acta*, 1991, **186**, 103–111.
7 Y. Ni, S. Chen and S. Kokot, *Anal. Chim. Acta*, 2002, **463**, 305–316.
8 H. A. Flaschka, *EDTA titrations: an introduction to theory and practice*, Elsevier, 2013.
9 H. Xue, L. Sigg and F. G. Kari, *Environ. Sci. Technol.*, 1995, **29**, 59–68.
10 B. Ngwack and L. Sigg, *Geochim. Cosmochim. Acta*, 1997, **61**, 951–963.
11 B. Nowack, F. Kari and H. Krüger, *Water, Air, Soil Pollut.*, 2001, **125**, 243–257.
12 J. Friedly, D. Kent and J. Davis, *Environ. Sci. Technol.*, 2002, **36**, 355–363.
13 C. Oviedo and J. Rodríguez, *Quim. Nova*, 2003, **26**, 901–905.
14 J. Hernández-Allica, C. Garbisu, O. Barrutia and J. M. Becerril, *Environ. Exp. Bot.*, 2007, **60**, 26–32.
15 M.-M. Wang, C.-C. Zhang and F.-S. Zhang, *Waste Manage.*, 2016, **51**, 239–244.
16 P. M. Mader, *J. Am. Chem. Soc.*, 1960, **82**, 2956–2961.
17 E. Rizkalla, O. El-Shafey and N. Guindy, *Inorg. Chim. Acta*, 1982, **57**, 199–205.
18 G. R. Buettner, T. P. Doherty and L. K. Patterson, *FEBS Lett.*, 1983, **158**, 143–146.
19 C. Bull, G. J. McClune and J. A. Fee, *J. Am. Chem. Soc.*, 1983, **105**, 5290–5300.
20 Y. W. Ebright, Y. Chen, P. S. Pendergrast and R. H. Ebright, *Biochem.*, 1992, **31**, 10664–10670.
21 A. Brausam and R. van Eldik, *Inorg. Chem.*, 2004, **43**, 5351–5359.
22 W. Li, C.-Z. Wu, S.-H. Zhang, K. Shao and Y. Shi, *Environ. Sci. Technol.*, 2007, **41**, 639–644.
23 P. Chakrabarti, F. M. Hatcher, R. Blake, P. A. Ladd and D. A. Blake, *Anal. Biochem.*, 1994, **217**, 70–75.
24 R. Bowman and J. Moir, *Soil Sci. Soc. Am. J.*, 1993, **57**, 1516–1518.
25 N. Azhar, M. Y. Ashraf, M. Hussain and F. Hussain, *Pak. J. Bot.*, 2006, **38**, 1551–1560.
26 L. Davidsson, A. Almgren and R. F. Hurrell, *J. Nutr.*, 1998, **128**, 1139–1143.
27 M. K. Islam, C. Tsuboya, H. Kusaka, S.-i. Aizawa, T. Ueki, H. Michibata and K. Kanamori, *Biochim. Biophys. Acta*, 2007, **1770**, 1212–1218.
28 H. Michibata, *Vanadium: biochemical and molecular biological approaches*, Springer Science & Business Media, 2011.
29 K. Kanamori, Y. Kinebuchi and H. Michibata, *Chem. Lett.*, 1997, 423–424.
30 M. S. Espinosa, R. Servant and P. A. Babay, *Microchem. J.*, 2016, **129**, 151–157.
31 S. Paston, A. Nikolaev and P. Ushkov, *J. Struct. Chem.*, 2017, **58**, 392–398.
32 J. Lati, J. Koresh and D. Meyerstein, *Chem. Phys. Lett.*, 1975, **33**, 286–288.
33 F. Neese and E. I. Solomon, *J. Am. Chem. Soc.*, 1998, **120**, 12829–12848.
34 M. C. Gennaro, P. Mirti and C. Casalino, *Polyhedron*, 1983, **2**, 13–18.
35 W. D. Wheeler and J. I. Legg, *Inorg. Chem.*, 1985, **24**, 1292–1297.
36 B. T. Khan and K. Annapoorna, *Inorg. Chim. Acta*, 1990, **176**, 241–246.
37 Y. Ba, S. Han, L. Ni, T. Su and A. Garcia, *J. Chem. Educ.*, 2006, **83**, 296.
38 J. Ryczkowski, *Vib. Spectrosc.*, 2000, **22**, 55–62.
39 Y. Zhao, C. Cai, Y. Luo and Z. He, *J. Supercond.*, 2004, **17**, 383–387.
40 K. Kanamori, H. Dohniwa, N. Ukita, I. Kanesaka and K. Kawai, *Bull. Chem. Soc. Jpn.*, 1990, **63**, 1447–1454.
41 C. C. Wagner and E. J. Baran, *Spectrochim. Acta, Part A*, 2010, **75**, 807–810.
42 T. Mizuta, J. Wang and K. Miyoshi, *Inorg. Chim. Acta*, 1993, **203**, 249–252.
43 J. D. Zubkowski, D. L. Perry, E. J. Valente and S. Lott, *Inorg. Chem.*, 1995, **34**, 6409–6411.
44 M. Lind, M. Hamor, T. Hamor and J. Hoard, *Inorg. Chem.*, 1964, **3**, 34–43.
45 C. Kennard, *Inorg. Chim. Acta*, 1967, **1**, 347–354.
46 T. Mizuta, T. Yamamoto, K. Miyoshi and Y. Kushi, *Inorg. Chim. Acta*, 1990, **175**, 121–126.
47 T. Schneppensieper, S. Seibig, A. Zahl, P. Tregloan and R. van Eldik, *Inorg. Chem.*, 2001, **40**, 3670–3676.
48 I. Ivanovic-Burmazovic, M. S. Hamza and R. van Eldik, *Inorg. Chem.*, 2002, **41**, 5150–5161.
49 I. Ivanović-Burmazović, M. S. Hamza and R. van Eldik, *Inorg. Chem.*, 2006, **45**, 1575–1584.
50 A. A. El-Sherif, M. M. Shoukry, W. M. Hosny and M. G. Abd-Elmoghny, *J. Solution Chem.*, 2012, **41**, 813–827.
51 X.-B. Wang, *J. Phys. Chem. A*, 2017, **121**, 1389–1401.
52 D. Hanstorp and M. Gustafsson, *J. Phys. B: At., Mol. Opt. Phys.*, 1992, **25**, 1773.
53 X.-B. Wang, Y.-L. Wang, J. Yang, X.-P. Xing, J. Li and L.-S. Wang, *J. Am. Chem. Soc.*, 2009, **131**, 16368–16370.
54 M. J. Frisch, G. W. Trucks, H. B. Schlegel, G. E. Scuseria, M. A. Robb, J. R. Cheeseman, G. Scalmani, V. Barone, B. Mennucci, G. A. Petersson, H. Nakatsuji, M. Caricato, X. Li, H. P. Hratchian, A. F. Izmaylov, J. Bloino, G. Zheng, J. L. Sonnenberg, M. Hada, M. Ehara, K. Toyota, R. Fukuda, J. Hasegawa, M. Ishida, T. Nakajima, Y. Honda, O. Kitao, H. Nakai, T. Vreven, J. A. Montgomery Jr., J. E. Peralta, F. Ogliaro, M. J. Bearpark, J. Heyd, E. N. Brothers, K. N. Kudin, V. N. Staroverov, R. Kobayashi, J. Normand, K. Raghavachari, A. P. Rendell, J. C. Burant, S. S. Iyengar, J. Tomasi, M. Cossi, N. Rega, N. J. Millam, M. Klene,

J. E. Knox, J. B. Cross, V. Bakken, C. Adamo, J. Jaramillo, R. Gomperts, R. E. Stratmann, O. Yazyev, A. J. Austin, R. Cammi, C. Pomelli, J. W. Ochterski, R. L. Martin, K. Morokuma, V. G. Zakrzewski, G. A. Voth, P. Salvador, J. J. Dannenberg, S. Dapprich, A. D. Daniels, O. Farkas, J. B. Foresman, J. V. Ortiz, J. Cioslowski and D. J. Fox, *Gaussian 09*, Gaussian, Inc., Wallingford, CT, USA, 2009.

55 D. Coskun, S. V. Jerome and R. A. Friesner, *J. Chem. Theory Comput.*, 2016, **12**, 1121–1128.

56 M. Walker, A. J. Harvey, A. Sen and C. E. Dessent, *J. Phys. Chem. A*, 2013, **117**, 12590–12600.

57 Y. Zhao and D. G. Truhlar, *Theor. Chem. Acc.*, 2008, **120**, 215–241.

58 X.-B. Wang and S. R. Kass, *J. Am. Chem. Soc.*, 2014, **136**, 17332–17336.

59 Y. Li and D.-C. Fang, *Phys. Chem. Chem. Phys.*, 2014, **16**, 15224–15230.

60 D. Gruzman, A. Karton and J. K. L. Martin, *J. Phys. Chem. A*, 2009, **113**, 11974–11983.

61 Y.-F. Yang, L. W. Chung, X. Zhang, K. N. Houk and Y.-D. Wu, *J. Org. Chem.*, 2014, **79**, 8856–8864.

62 T. Lu and F. Chen, *J. Comput. Chem.*, 2012, **33**, 580–592.

63 X.-B. Wang, B. Jagoda-Cwiklik, C. Chi, X.-P. Xing, M. Zhou, P. Jungwirth and L.-S. Wang, *Chem. Phys. Lett.*, 2009, **477**, 41–44.

64 T. Polynova, L. Zasurskaya and A. Ilyukhin, *Crystallogr. Rep.*, 1997, **42**, 155–157.

65 W.-S. Jung, Y. K. Chung, D. M. Shin and S.-D. Kim, *Bull. Chem. Soc. Jpn.*, 2002, **75**, 1263–1267.

66 S. Matsuo, K. Shirozu, Y. Tateishi, H. Wakita and T. Yokoyama, *Adv. Quantum Chem.*, 2003, **42**, 407–417.

67 G. Murdachaew, M. Valiev, S. M. Kathmann and X.-B. Wang, *J. Phys. Chem. A*, 2012, **116**, 2055–2061.

68 X.-B. Wang and L.-S. Wang, *J. Chem. Phys.*, 2000, **112**, 6959–6962.

69 X. Yang, X.-B. Wang, L.-S. Wang, S. Niu and T. Ichiye, *J. Chem. Phys.*, 2003, **119**, 8311–8320.

70 S. W. Wren, K. M. Vogelhuber, T. Ichino, J. F. Stanton and W. C. Lineberger, *J. Phys. Chem. A*, 2012, **116**, 3118–3123.

71 X.-P. Xing, X.-B. Wang and L.-S. Wang, *J. Phys. Chem. A*, 2008, **113**, 945–948.

72 *CRC Handbook of Chemistry and Physics*, ed. D. R. Lide, 2012.

73 K. Kanamori, M. Sakurai, T. Kinoshita, T. Uyama, T. Ueki and H. Michibata, *J. Inorg. Biochem.*, 1999, **77**, 157–161.